The Astrophysical Journal, 651:1219–1228, 2006 November 10

MODELING THE RADIATIVE SIGNATURES OF TURBULENT HEATING IN CORONAL LOOPS

S. Parenti[1]
Institut d'Astrophysique Spatiale, Batiment 121, F-91405 Orsay, France; s.parenti@oma.be

E. Buchlin[2]
Dipartimento di Astronomia e Scienza dello Spazio, Università di Firenze, Largo E. Fermi 2, 50125 Florence, Italy

P. J. Cargill
Space and Atmospheric Physics, Blackett Laboratory, Imperial College, London SW7 2BZ, UK

and

S. Galtier and J.-C. Vial
Institut d'Astrophysique Spatiale, Batiment 121, F-91405 Orsay, France; and Université Paris-Sud 11 and CNRS (UMR 8617)
Received 2006 February 22; accepted 2006 July 11

ABSTRACT

The statistical properties of the radiative signature of a coronal loop subject to turbulent heating obtained from a three-dimensional (3D) magnetohydrodynamics (MHD) model are studied. The heating and cooling of a multistrand loop is modeled and synthetic spectra for Fe xii 195.12, Fe xv 284.163, and Fe xix 1118.06 Å are calculated, covering a wide temperature range. The results show that the statistical properties of the thermal and radiative energies partially reflect those of the heating function in that power-law distributions are transmitted, but with very significant changes in the power-law indices. There is a strong dependence on the subloop geometry. Only high-temperature radiation ($\approx 10^7$ K) preserves reasonably precise information on the heating function.

Subject headings: methods: statistical — MHD — Sun: corona — Sun: flares — Sun: UV radiation — techniques: spectroscopic — turbulence

1. INTRODUCTION

The coronal heating problem is concerned with identifying the energy dissipation process(es) that lead to coronal temperatures well in excess of 10^6 K (see, for example, Mandrini et al. 2000; Klimchuk 2006). A complete model of the corona needs to be able to simulate not only the physical mechanisms for energy input and dissipation, but also the plasma response to heating and possible observables that can benchmark the model. In general, the problem is often broken up into discrete parts; in particular, energy dissipation and transport are usually treated as independent problems (but see the recent work of Peter et al. 2004; Gudiksen & Nordlund 2005).

Impulsive coronal heating, as originally discussed by Lin et al. (1984) and Parker (1988), is a potentially viable model for closed-field regions. Energy is dissipated through discrete impulsive events over small scales, both in space and energy. The number of flares and microflares is distributed in energy as a power law having an index somewhat more positive than -2 (see Crosby et al. 1993; Aschwanden & Parnell 2002, for a review), and Hudson (1991) further argued that if smaller (perhaps unresolved) events such as nanoflares are to heat the corona, the index should be more negative than -2. Studies on the line intensity also show similar distributions (Berghmans et al. 1998; Aletti et al. 2000; Buchlin et al. 2006). Studies of the energy distribution of smaller events (referred to hereafter as nanoflares, although in fact the energy can be in a wide range) rely on estimates of the amount of energy associated with the radiation of an observed X-ray and ultraviolet (XUV) or EUV brightening (e.g., Berghmans et al. 1998; Aschwanden et al. 2000; Parnell & Jupp 2000). A range of indices are obtained, with values both greater than and less than -2 (Parnell 2004). A basic assumption of this approach is that one can associate the same statistical properties in the distributions of the injected and radiated energies so that the plasma response simply transmits the distribution of the nanoflares as opposed to modifying it. However, this hypothesis has never actually been tested.

This paper carries out such a test using a forward-modeling approach. In general terms, forward modeling uses a model of the corona to generate "observables," which can then be compared with what is actually observed. This enables one to study the role of effects that may be difficult to pin down from the observations, such as the geometry of the observed structure, line of sight, assumption of ionization equilibrium, and elemental composition, to name a few examples. In the context of this paper, the technique can be used to simulate the coronal response to a prescribed nanoflare distribution with a range of energies, some of which may be unresolvable as individual events.

The key step linking the input nanoflare energy distribution and the output distribution of "events" as seen in various emission lines is understanding how the coronal plasma responds to impulsive heating, since the temperature, density, and velocity determine the intensity of the spectral lines we calculate. So, the question we address is: for a given distribution of input energies, how does coronal energy transport determine the energy distribution of measured events? There has been extensive modeling of the coronal response to nanoflare energy input in recent years (see, for example, Peres 2000; Mendoza-Briceño et al. 2004 2005; Winebarger & Warren 2004; Testa et al. 2005; Patsourakos et al. 2004; Patsourakos & Klimchuk 2006; Klimchuk 2006 for a discussion and further references). However, these models consider nanoflare heating to be repeated either in a single

[1] Current address: Royal Observatory of Belgium, 3 Avenue Circulaire, B-1180 Brussels, Belgium.
[2] Current address: Space and Atmospheric Physics, Blackett Laboratory, Imperial College, London SW7 2BZ, UK.

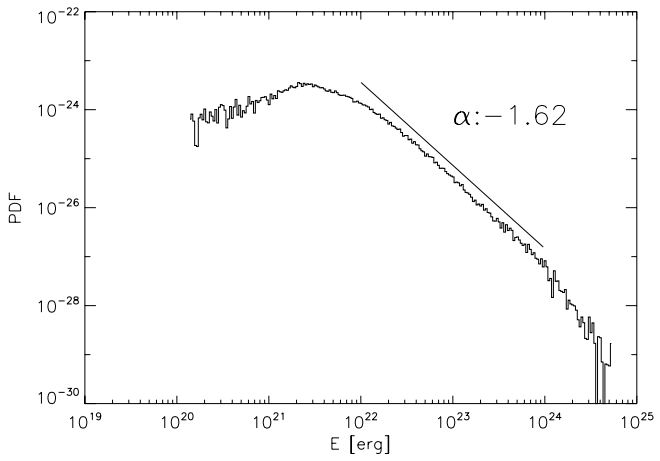

FIG. 1.—PDF for the nanoflare energy (the average value is 1.2×10^{24} ergs) heating the loop system.

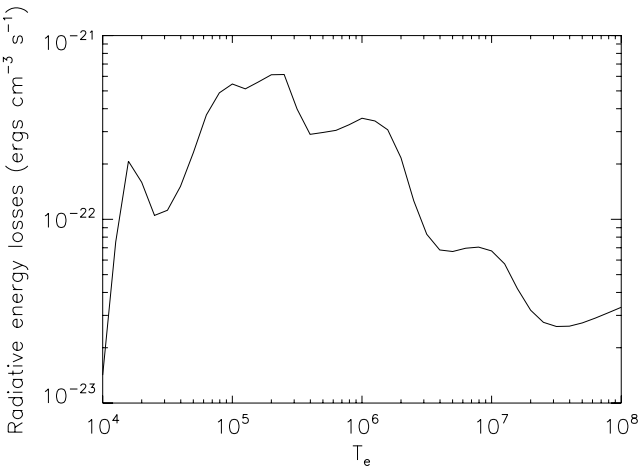

FIG. 2.—Radiative-loss function as a function of temperature derived using the CHIANTI database.

monolithic loop or in a few strands. Here, as described in § 2, we assume a highly fragmented corona and consider each observed loop to be comprised of many small strands.

The paper is organized as follows. Section 2 (and the associated Appendix B) describes the models for the nanoflare energy distribution (a 3D MHD model) and the energy-response model. Section 3 describes the distribution of coronal thermal energy for the nanoflare input, and § 4 presents the properties of synthetic spectra.

2. THE MODEL

We adopt an approach of using a model of coronal turbulence to generate a distribution of nanoflare energies, and a second model to calculate the response of the coronal temperature and density to heating by such nanoflares.

2.1. *The Heating Model*

To generate the distribution of nanoflare energies we use a 3D hybrid model of MHD turbulence from Einaudi & Velli (1999) and Buchlin et al. (2003) that simulates the coronal effects of photospheric turbulent motion at the loop footpoints. These random motions cause the propagation of Alfvén waves along the loop, first producing storage, and then impulsive dissipation of magnetic energy. The time-dependent dissipation then gives the heating function used here. Further details on the model are provided in the Appendices A and B. The probability distribution function (PDF) of the dissipated energy is a clear power law with index close to -1.6 over about 2 decades (Fig. 1). Such power-law behavior seems to be common to self-organized critically (SOC) systems, which involve a spontaneous organization of the system into a critical state under the action of small external disturbances, leading to energy dissipations over many scales. We also see falloffs at high and low energies, which are caused by the upper and lower current thresholds imposed for the energy dissipation in the model. Because the purpose of the present work is to verify how the power law is transmitted by the plasma response, our investigation focuses on the central part of the energy distribution. In §§ 3 and 4 we use this distribution such that the average energy values vary between 6×10^{23} and 1.2×10^{25} ergs, depending on the simulation. Each distribution has energy varying over almost 5 decades (Fig. 1, for example).

2.2. *The Cooling Model*

To study the plasma response to this kind of heating, we assume that the timescale for energy input is short compared to the characteristic cooling time of the corona by conduction or radiation. Typical cooling times are a few hundred to over a thousand seconds, so this seems reasonable. Cooling of coronal plasmas has been well studied for many years (see Cargill et al. 1995 for a review of early work and Walsh & Galtier 2000; Winebarger & Warren 2004; Reale et al. 2005; Bradshaw & Cargill 2005 for more recent efforts). A coronal loop cools by conduction and radiation with characteristic timescales

$$\tau_c = \frac{5}{2}\frac{pL^2}{kT_e^{7/2}}, \quad \tau_r = \frac{3kT_e^{1-\beta}}{N_e\chi}, \tag{1}$$

where p is the plasma pressure, $\Lambda(T_e) = \chi T_e^{\beta}$ is the loss function (we used a parameterization of the curve shown in Fig. 2), and k is the Boltzman constant. Analysis of these timescales show that an impulsively heated loop will cool first by conduction (high temperature, low density), with an associated "evaporation" of chromospheric plasma, and subsequently by radiation with plasma draining (low temperature, high density), as demonstrated in both analytical and numerical models.

In the present work, we wish to model an "observed" coronal loop as being highly fragmented, composed of many small, unresolved strands. For example, a loop with an observed diameter of 10″ may have 10^4–10^6 strands of scales 10–100 km. If each of these strands is heated independently, one is required to follow the cooling of a lot of strands. For this reason we use the analytical multistrand model first developed by Cargill (1994), as opposed to full solutions of the energy-transport equations. The details of this model are in Appendix B. We thus consider a coronal "loop" comprised of ($N \gg 1$) identical elemental strands (the cases $N = 500$ and 5000 are shown), each strand having the same cross-sectional area A_h and semilength L. The values assumed for L and the loop section ($N \times A_h$) are typical values derived from EUV observations (e.g., 10^9 cm and 10^{14} cm^2). As discussed later, the number of strands is chosen to study different cases of low– and high–filling-factor loops.

At the beginning of the simulation all strands are cool and empty. Each strand is described by one temperature T_e and one density N_e. Each nanoflare is instantaneous and heats only one strand, randomly chosen inside the loop. This energy all goes into plasma heating. The heating function is described by the power law in energy discussed in § 2.1, and is distributed randomly (i.e., which strand is heated is determined by a random

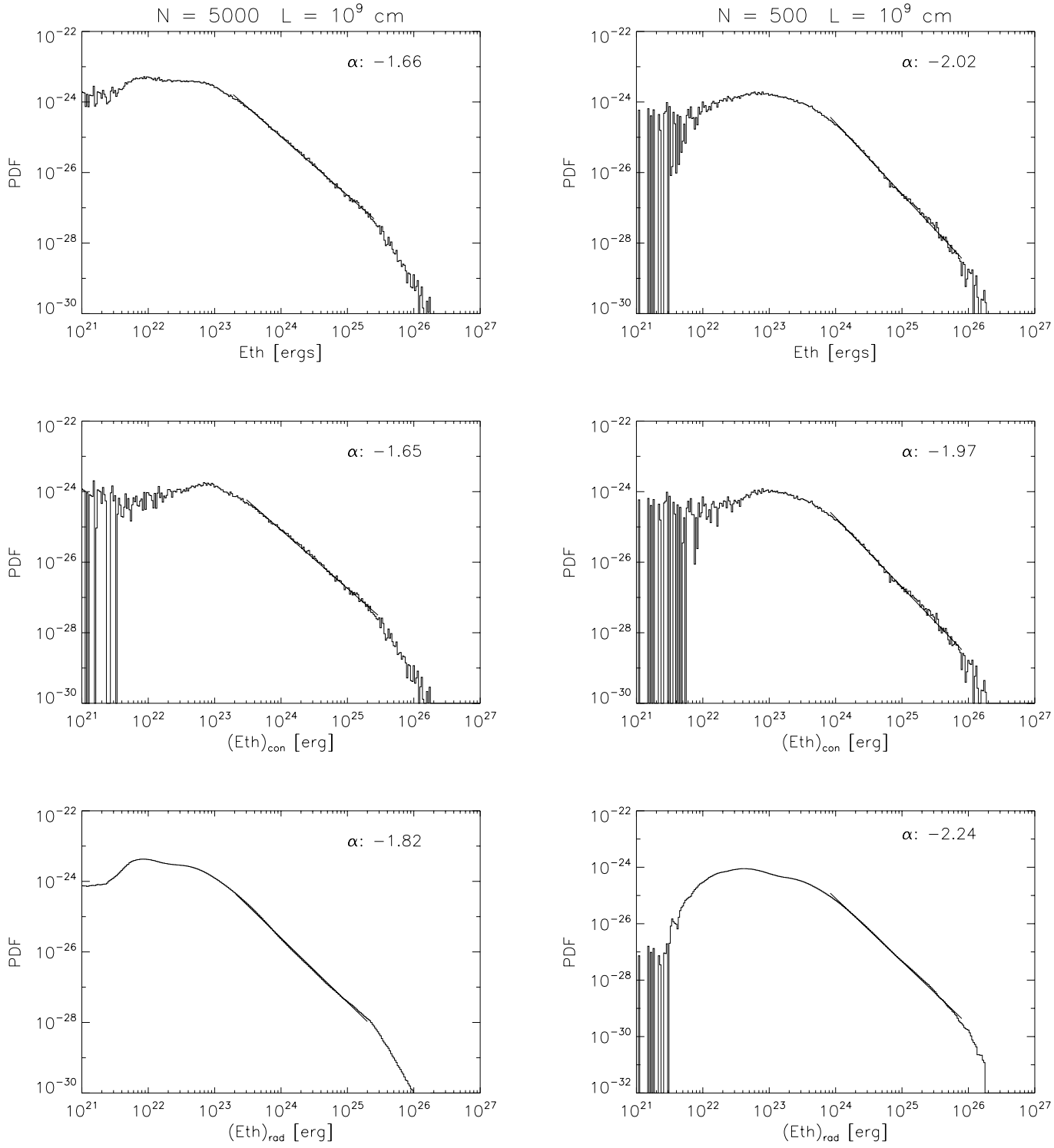

FIG. 3.—PDFs of total thermal energy (*top*); PDFs for the thermal energy during the conductive cooling phase (*middle*); and the PDF of the thermal energy during the radiative cooling phase (*bottom*). *Left*: $A_h = 8 \times 10^{13}$ cm^2, $N = 5000$. *Right*: $A_h = 8 \times 10^{14}$ cm^2, $N = 500$. For both cases $L = 10^9$ cm. The index of the fitted power law is represented by α.

number generator). Unlike earlier publications using this model, we replace the simple radiative loss function with a parameterization of the one available in the CHIANTI version 4.2 atomic database (Young et al. 2003). This function was calculated assuming the Mazzotta et al. (1998) ionization equilibrium and coronal abundances. The same assumptions are made later on to build the synthetic spectra.

3. DISTRIBUTIONS OF THERMAL ENERGY IN RESPONSE TO A POWER-LAW ENERGY INPUT

In this section we investigate the PDF of the loop thermal energy generated by the MHD model. The temperature and density in each strand are obtained as a function of time from the cooling model, and the PDF of the thermal energy is obtained

by summing all the strands. Two cases are shown, with the number of elemental strands being different in each. They correspond to low and high filling factors, where the filling factor is a measure of what fraction of any (unresolved) coronal volume is actually filled with radiating plasma. For simplicity, the filling factor is defined as the ratio of the number of hot strands ($\log T > 5$) to the total number of strands (see Cargill [1994] for more details). The filling factor is important because for low (high) values, one tends to heat cool, low-density (hot, high-density) strands. It also measures the characteristic "repeat time" of strand heating relative to the cooling time. When the characteristic timescale of the strand cooling is much shorter than the inverse frequency of injection of nanoflares in the loop, the filling factor is small and the strand is scarcely visible at coronal temperatures.

The top two panels of Figure 3 show the PDF of the thermal energy of our loop with a low– (high–) filling-factor case on the left (right). All phases of the cooling are included in the PDF. The left panels show the case $A_h = 8 \times 10^{13}$ cm^2, $N = 5000$ (filling factor of 0.06), and the right panels have $A_h = 8 \times 10^{14}$ cm^2, $N = 500$ (filling factor of 0.52). In both cases the energy loss is 5×10^{-4} ergs cm^{-3} s^{-1} and $L = 10^9$ cm. We have fit the thermal energy distribution by a power law with slope α in the vicinity of 10^{24}–10^{25} ergs. It is clear that the generic power-law distribution of the heating function is transmitted to the thermal energy over about two decades. However, α depends on the strand geometry, with the absolute value of α (the term we will now use) increasing for wider strands. (Note that at the lower and upper extremes the PDF deviates due to the model limitations discussed in § 2.1. In particular, the low-energy distribution is likely to be unphysical.)

We then analyzed the PDFs from the conductive and radiative cooling phases separately (middle and bottom panels in Fig. 3, respectively). As expected, both components follow a power-law distribution, but the radiative phase is steeper. For small filling factors (*left panels*), the total PDF and that of the conduction phase are very similar, suggesting that information about the energy input is directly transmitted at high temperatures. The dependence on filling factor in the conductive phase can be understood as follows. For low filling factors, the initial thermal energy in the strand is proportional to the nanoflare energy, and the evaporative cooling takes place at constant pressure (or constant thermal energy; Antiochos & Sturrock 1978). Hence, the nanoflare distribution will map precisely into that of the thermal energy. In the high–filling-factor case, any one strand is subject to sporadic but inevitable reheating, which prevents the strand from completing its cooling cycle (note the lack of the very low energy component in the radiative PDF for high filling factors). Each time the strand is reheated while it is still cooling from the previous nanoflare, its temperature increases and makes the thermal energy associated with the previous nanoflare jump to higher values. For this reason the PDF changes its shape. Such change particularly involves the low-intermediate energies and makes the index α increase. This is because the reheating has a higher probability of happening over a strand preheated by a small-intermediate energy flare.

In the radiative phase, the PDF is more complex for several reasons. At this time the thermal energy decreases as $T^{1-\beta}$, which leads to an enhancement of the low-energy part of the PDF. The complex dependence of the radiative cooling on the temperature leads to the nonuniformity. [We performed several tests in which we assumed a single value of $\beta(=-\frac{1}{2})$. A single power law was then found over a wider energy range.] However, it is clear that this leads to a lack of perfect "transmission" of the input energy distribution.

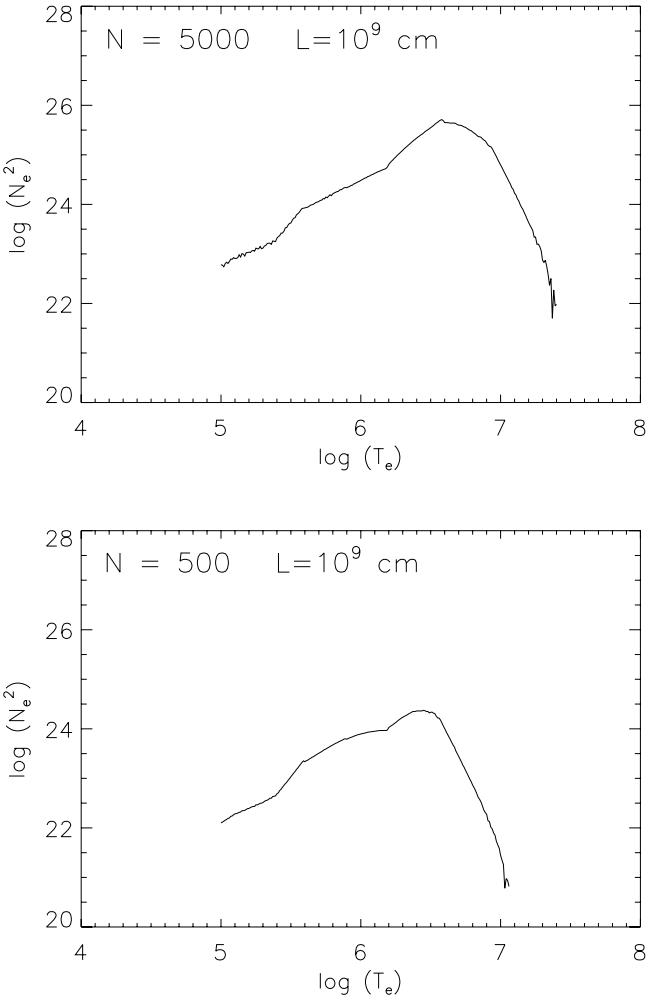

FIG. 4.—Logarithm of N_e^2 as a function of the logarithm of temperature, obtained with the parameters $A_h = 8 \times 10^{13}$ cm^2, $N = 5000$ (*top*) and $A_h = 8 \times 10^{14}$ cm^2, $N = 500$ (*bottom*).

4. PDFs OF SYNTHETIC SPECTRA

The next step is to generate synthetic spectra arising from the combined heating and cooling models. For the present work we chose to synthesize the Fe XII 195.12 ($\log T_{\max} = 6.14$), Fe XV 284.163 ($\log T_{\max} = 6.3$), and Fe XIX 1118.06 Å ($\log T_{\max} = 6.9$) line intensities. The first two lines are observed by the *Solar and Heliospheric Observatory* (*SOHO*) EUV Imaging Telescope (EIT; Delaboudiniere et al. 1995) and will be observable by the *Solar-B* EUV Imaging Spectrometer (EIS), which will be launched in 2006. These are background, relatively hot and bright resonant lines in the corona. Fe XIX is a much hotter line that can be observed by *SOHO* Solar Ultraviolet Measurement of Emitted Radiation (SUMER; Wilhelm et al. 1995). The choice of such lines is guided by the intention of covering medium-high coronal temperatures.

A line intensity is defined as

$$I_\lambda = \frac{1}{4\pi} \int G(T_e) N_e^2 dh, \qquad (2)$$

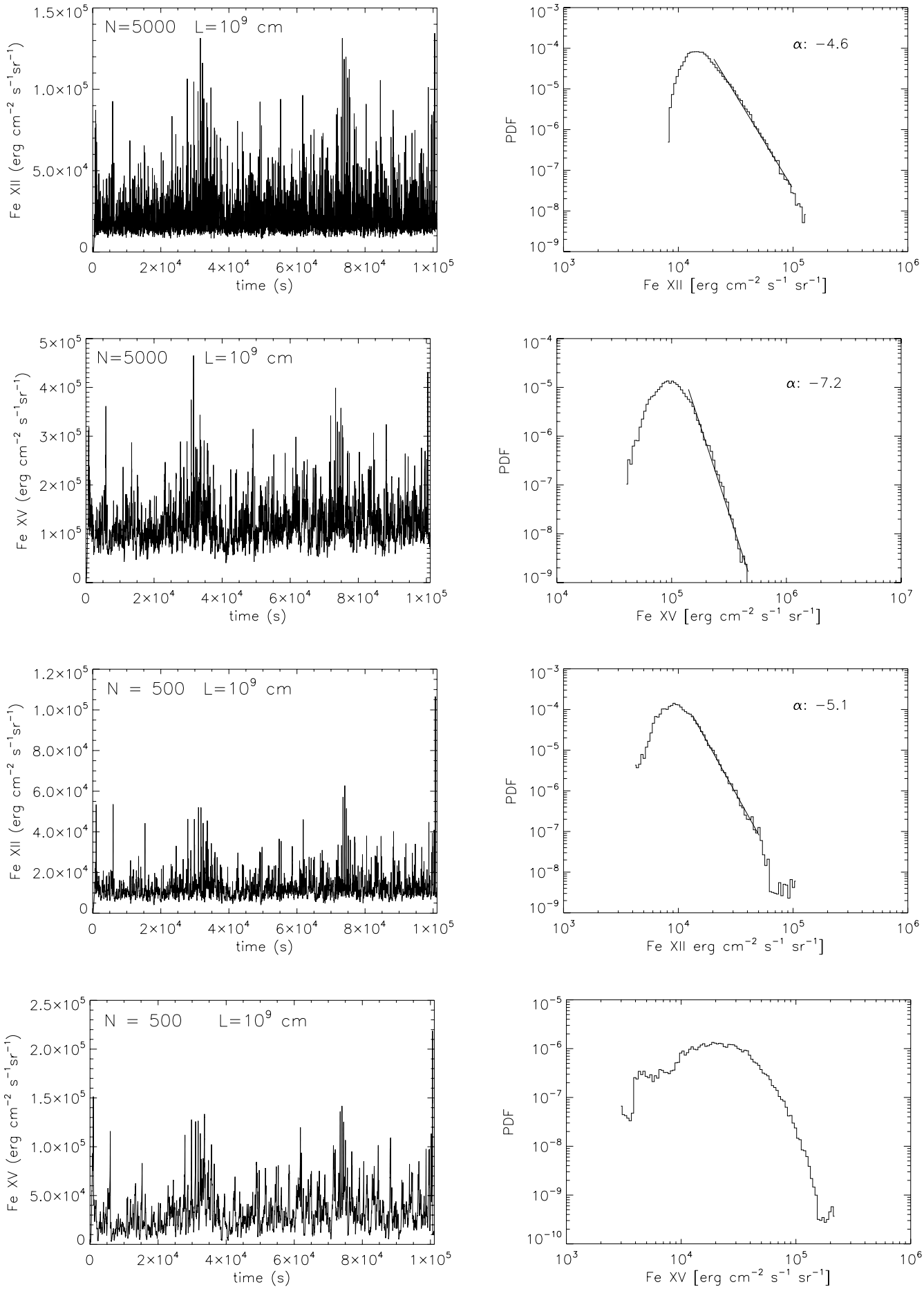

FIG. 5.—Total loop intensity as a function of time (*left*) for Fe XII 195 Å (*first and third panels*) and Fe XV 284 Å (*second and fourth panels*) and their PDFs (*right*). The parameters used for the simulation are the same as in Fig. 4.

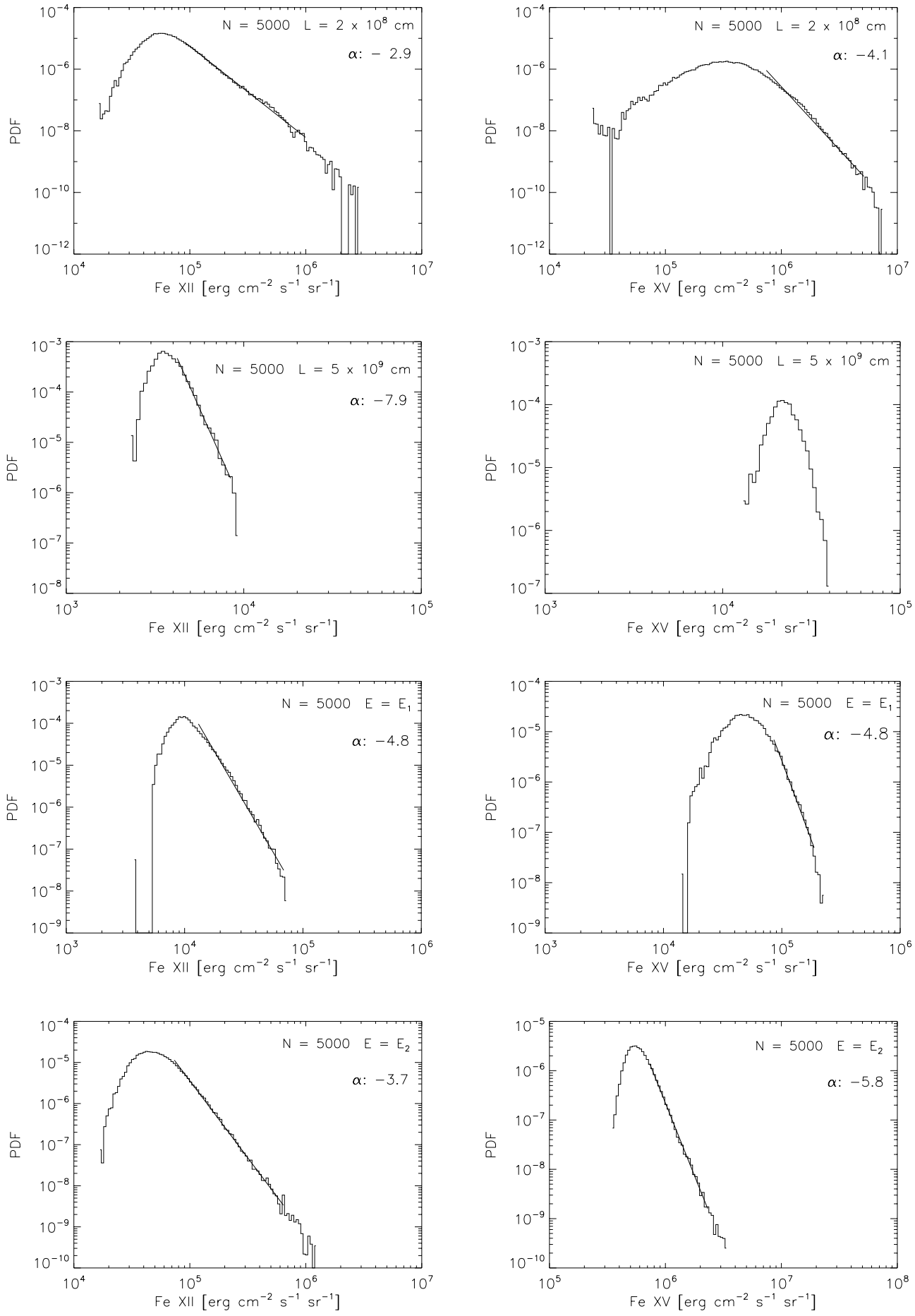

FIG. 6.—PDFs for Fe XII 195 Å (*left*) and Fe XV 284 Å (*right*). PDFs for different values of L (*top four panels*) and flare energy (*bottom four panels*). Here $E_1 = 2.5 \times 10^{-4}$ ergs cm^{-3} s^{-1} and $E_2 = 5 \times 10^{-3}$ ergs cm^{-3} s^{-1}.

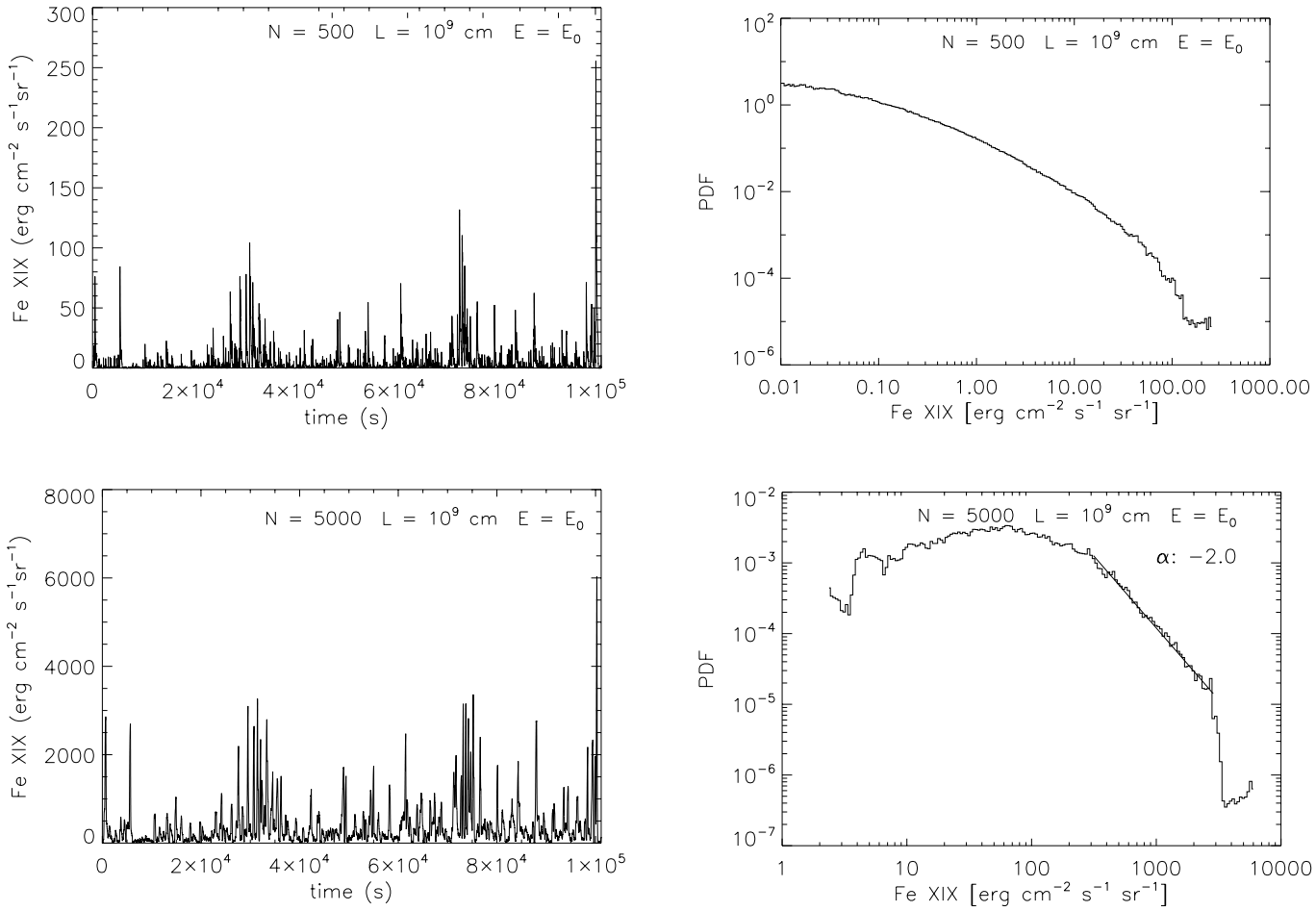

FIG. 7.—Total loop intensity as a function of time (*left*) for Fe XIX 1118 Å and the corresponding PDF (*right*). The loss energy is assumed to be $E_0 = 5 \times 10^{-4}$ ergs cm^{-3} s^{-1}.

where $G(T_e)$ is the contribution function, which gives information on the distribution of the line emission in temperature and the plasma density N_e along the line of sight h. The contribution functions were calculated with the CHIANTI database providing coronal abundances. To generate the line intensities we use the density and temperature histories of each strand and calculate the total loop time-dependent line intensity.

The distribution of the emission measure (EM, which scales as $N_e^2 V$) as a function of temperature will be important in understanding our results. The EM distributions peak in the range $\log T_{\max} = 6.4$–7.2, assuring important emission from the chosen lines. Figure 4 shows two examples of the distribution of N_e^2 as a function of temperature, using the same parameters as Figure 3. These results were obtained by summing the densities of all the strands for each temperature interval of the loop. Because in the model the temperature is assumed to be uniform along a strand, and all the strands have the same volume, the quantity plotted in Figure 4 is representative of the total loop EM. There is a broad range of temperatures (a lower limit $\log T_e = 5$ was imposed) that reflect the presence of many strands at different states of cooling. As pointed out by Cargill (1994), the case with smaller filling factor (*top panel*) has more plasma at higher temperature.

The left-hand panels in Figure 5 show examples of the time variation of Fe XII and Fe XV intensities, in which the same parameters as in Figures 3 and 4 are used. The two top (bottom) panels show cases with low (high) filling factors. Larger strand cross sections give smaller values of the intensity (note the drop in the EM at coronal temperatures) with smaller frequency fluctuations. The PDFs shown in the right column also demonstrate this. Like the thermal energy, the intensity distributions show a power-law distribution. However, these PDFs have entirely different power-law indices from the heating function; indeed, a power law is not evident in the bottom right panel (Fe XV with large filling factor). Thus, at these temperatures information of the energy input does not seem to have survived.

For the low–filling-factor loop shown in Figure 5 (*top panels*), the PDF index increases for the higher temperature line. This result comes about because of the location of the peak formation temperature of the line with respect to the EM-T distribution plotted in Figure 4. There are two aspects to consider. First, the formation temperature of these lines falls on the left side of the maximum of the EM. This means that the lines form when the strand is cooling by radiation, far from the initial heating, and so suffering from amnesia. Moreover, looking at the top panel of Figure 4, we see that these two lines form at temperatures where the gradients of the EM distributions are different. This means that the temperatures around the peak emission of each line contribute in a different way to the line intensity.

The top four panels of Figure 6 show the PDFs for Fe XII (*left panels*) and Fe XV (*right panels*), and are for cases where the loop cross section and input energy are held fixed (at the values of the top panels in Fig. 5), and the loop length is varied. In the top two panels we take $L = 2 \times 10^8$ cm (filling factor of 0.013),

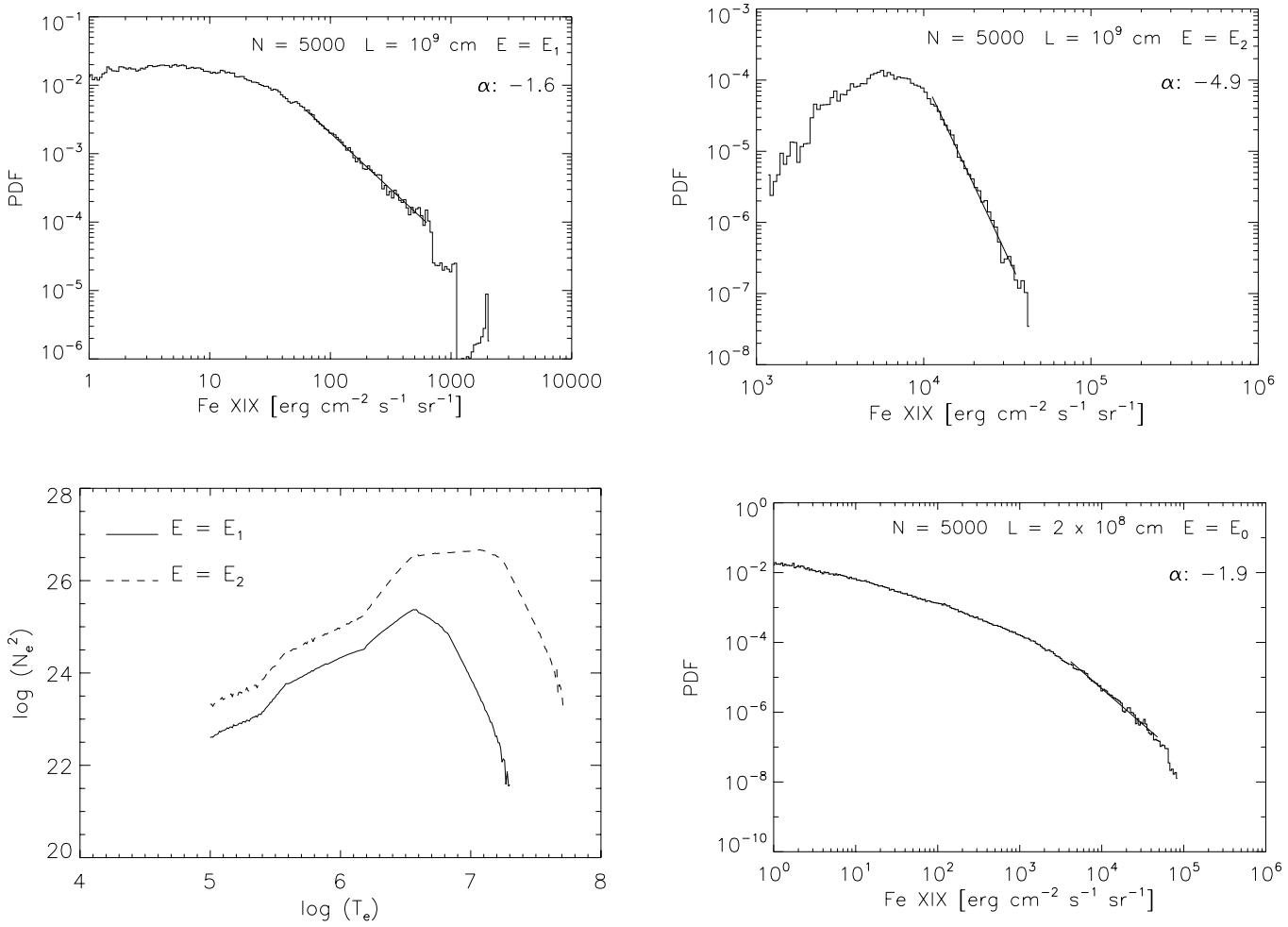

FIG. 8.—*Top*: PDFs for Fe XIX assuming an energy loss of $E_1 = 2.5 \times 10^{-4}$ ergs cm^{-3} s^{-1} and $E_2 = 5 \times 10^{-3}$ ergs cm^{-3} s^{-1}. The respective EMs are given in the bottom left panel. *Bottom right*: PDF for Fe XIX, assuming the same parameters of Fig. 7 bottom, but with a different value of L.

while in the second two panels we take $L = 5 \times 10^9$ cm (filling factor of 0.86). This provides further confirmation that for each line, the smallest filling factor is associated with the smaller power-law index. (The smaller filling factor is obtained because the thermal-conduction cooling time scales with L^2, while the number of flares remains the same in all the cases discussed here. As the cooling time decreases, it increases the number of strands that cool completely before being reheated.)

The plots in the third and fourth rows of Figure 6 were obtained by changing the nanoflare energy while keeping the rate of nanoflares and the loop parameters constant. In particular, we assumed $N = 5000$, $L = 10^9$ cm, and $A_h = 8 \times 10^{13}$ cm^2. A smaller value of the nanoflare energy has the effect of decreasing the temperature of the peak of the EM. While in the previous cases the average flare energy was 1.2×10^{24} ergs, here we used 6×10^{23} ergs (E_1 in the third row of the figure) and 1.2×10^{25} ergs (E_2 in the last row of the figure). In the third row we obtain a filling factor of 0.07, which is quite similar to the case shown in the top row of Figure 5. What we observe is a small change in the PDF of Fe XII, while Fe XV has almost lost its power-law shape. This can be explained by the small amount of plasma that is left at the Fe XV temperatures. In the bottom row of Figure 6, we show the PDFs for a higher value of the nanoflare energy. For this case the EM extends to quite high temperatures ($\log T = 7.6$; see also the EM in Fig. 8). The filling factor is 0.043, and there is enough plasma for the emission of Fe XV, which again shows a power-law distribution. These last two results point out the importance of the "right" choice of the temperature interval to investigate.

We now investigate the behavior of the Fe XIX intensity for all the loop conditions discussed thus far. The results are shown in Figures 7 and 8. In Figure 7 the plots were obtained assuming the same parameters as Figure 4 and 5. The top case is for the high–filling-factor loop. Here there is not enough material at the peak Fe XIX formation temperature to guarantee any detectable emission. This also produces a shallow PDF.

In the second case, the PDF shows a power-law distribution with an index close to that of the heating function. Here the formation temperature of the line falls very close to (on the right side) the maximum of the EM-T distribution (see Fig. 4, *top*). This point corresponds to the plasma conditions at the moment when the strand is changing its cooling mode from conduction to radiation. Because the line formation temperature is just at the side of such peak, we can say that the line forms mainly while the strand is cooling by conduction, although there will be a radiative contribution.

The top left panel of Figure 8 shows the case when the line forms completely during the conduction cooling phase. Here we find the same index as the one for the energy input. This PDF, as well as that on the right side, was obtained by changing the energy

input (the same cases of Fig. 6) and keeping the flaring rate constant. As we mentioned before, a decrease in the input energy leads to a decrease in the temperature at which the density distribution peaks. This is shown in the bottom left panel of Figure 8 (*solid line*), where we reported the density distributions for the two cases just mentioned. As a consequence, the Fe XIX formation temperature falls in the range where the strand cools only by conduction. In the top right panel of Figure 8 we are in the opposite situation. The increase of the input energy produces an increase of material at higher temperatures. At the same time, the peak of the density distribution transforms into a plateau (*dashed curve*, *bottom left panel*). This is an indication that at such temperatures each strand is in a different phase of cooling. The Fe XIX temperature formation falls on such plateau, where strands in the conduction and radiation phases coexist. As a result, the index of the PDF steepens again.

The bottom right panel of Figure 8 shows the PDF for a lower filling-factor loop (same case as the top row of Fig. 6) than the previous examples. Here the conduction cooling time is much reduced with respect to the previous cases, so that the strand spends a short time at the temperature of emission of this line. For this reason, very little is left of the power-law distribution of the PDF (eventually only in the highest decade of intensity).

5. SUMMARY AND CONCLUSION

In this paper we have presented a simple model that is able to address the plasma response to heating in a highly structured corona. We use as input an energy distribution provided by a three-dimensional MHD model for coronal dissipation that has a well-defined power-law distribution of event energy. The thermal energy of the many strands comprising the structured corona is calculated, and distributions of thermal energy and line intensities can be calculated. Thus, this paper represents an important step in merging MHD and energy-transport models.

It was first demonstrated that the information contained in the statistics of the energy input to the coronal plasma can only be partially recovered in the statistics of thermal energy. The agreement between input and output distributions was better for cases of a low–filling-factor loop and at temperatures for which conductive cooling was dominant. However, the agreement was by no means exact, indicating that energy-transport processes gradually wash out the initial information.

An investigation of the distribution of the line intensities of a number of important coronal lines gave similar conclusions. However, an encouraging aspect of such a diagnostic is the different behaviors of lines that form at different temperatures. This can be interpreted as an indication that we need to look at hot coronal lines ($\approx 10^7$ K) in order to see a signature of the heating. The "right" temperatures to investigate seem to be those for which the thermal conduction is dominant over radiation as the cooling mechanism. At such high temperatures probably only newly heated strands emit, and the heating signature is not hidden by the averaging effects that are present when we look at lower temperatures. Observing at the Fe XII and Fe XV temperatures, we look at the million-degree background corona emission as the result of the cooling of a large number of strands, each of them in a different plasma condition. It is this "average" effect that is responsible for the large index in the intensity power law (the distribution of the average of a quantity tends toward a Gaussian distribution, which means an infinite power index).

In view of our results we stress the importance of investigating high-temperature lines, both from the theoretical and observational aspects. In particular, it is essential to use spectroscopic data (such as those of the new mission *Solar-B*, with good spatial and spectral resolutions) to better isolate the high-temperature components in the observed emission.

S. P. and E. B. would like to thank Marco Velli and Giorgio Einaudi for the original loop cellular automaton and for their valuable help using it and analyzing its results. S. P. also wishes to thank Jim Klimchuk for the encouragement and the fruitful discussions. S. P. and E. B. were supported through the TOSTISP European network contract HPRNCT 200100310. S. P. also acknowledges the support from the Belgian Federal Science Policy Office through the ESA-PRODEX program. CHIANTI is a collaborative project involving the NRL (USA), the RAL (UK), and the following universities: University College London (UK), Cambridge (UK), George Mason (USA), and Florence (Italy).

APPENDIX A

THE HEATING MODEL

The heating model was introduced in § 2.1, and full details can be found in Buchlin et al. (2003), especially § 2.2 of that paper. A coronal magnetic loop is modeled in a 3D simulation box. A background magnetic field points along the loop (defined as the z direction, so that $\boldsymbol{B}_0 = B_0 \hat{e}_z$), with the photosphere located at $z = 0,\ 2L$. The boundary conditions there impose a velocity field that models the stirring of the loop footpoints by photospheric motions. The energy introduced is then transferred into the rest of the loop by Alfvén waves. These waves interact through nonlinear interactions that are confined to the x-y plane. Energy release occurs in each of these planes and is modeled using a threshold technique, leading to avalanches of the fields. The model is intermediate between cellular automata (CA) and MHD models, and runs fast enough for a statistical analysis of the time series of energy dissipation in a turbulent loop, while keeping fields consistent with the equations of MHD.

The avalanche process is similar to CA models, such as those proposed by Lu & Hamilton (1991), but the threshold variable is the electric current density instead of the magnetic field gradient, and the magnetic field is updated using Maxwell's equations in a self-consistent manner. Thus, if the electric current density exceeds some given threshold at a point, the local current and vorticity are redistributed and the process is repeated until the threshold criterion is not met anywhere anymore, i.e., until the avalanche stops. The energy lost during this process is recorded, and we thus get a time series of energy dissipations.

To interface this model with the loop cooling hydrodynamic model described next, we selected the energy dissipated in one of the planes in the simulation box. Such energy has a power-law distribution, as described in § 2.1. One of the timescales for this heating model is the Alfvén speed (v_a), which defines the propagation time needed by the wave to propagate from one plane to the next. For our simulations, we assumed $v_a = 10^8$ cm s^{-1} ($B_0 = 10^{-3}$ T). The time step is then 3 s, which corresponds to the lapsed time between nanoflares in our hydrodynamic model.

APPENDIX B

THE HYDRODYNAMIC MODEL

After rapid heating by nanoflares, each loop strand cools as described by the energy equation

$$\frac{\partial p}{\partial t} + V_s \frac{\partial p}{\partial s} = -\gamma p \frac{\partial V_s}{\partial s} + (\gamma - 1)\left[\frac{\partial}{\partial s}\left(k_0 T_e^{5/2} \frac{\partial T_e}{\partial s}\right) - N_e^2 \Lambda(T_e)\right], \tag{B1}$$

where V_s is the plasma field-aligned flow, s is the coordinate along the magnetic field, k_0 is the thermal conductivity coefficient, and $\Lambda(T_e)$ is the optically thin radiative-loss function. The initial temperature and density immediately after the nanoflare are determined using energy conservation considerations based on the nanoflare energy, strand volume, and preheating state of the loop. For heating of an "evacuated" strand, it is assumed that the initial evaporation phase occurs rapidly with fast thermalization (see Cargill & Klimchuk [2004] for details).

The cooling model used is described fully in Cargill (1994) and Cargill & Klimchuk (1997). The key assumption is that, because of the strong dependence of the radiative and conductive cooling times on loop temperature (the ratio scales as approximately T^6 at constant pressure), we can treat the conductive and radiative cooling separately. This in fact enables us to use analytical models for each stage.

The loop cools first by conduction, where the solution of Antiochos & Sturrock (1978) for subsonic upflow of chromospheric material at constant pressure is used:

$$T_e(t) = T_0\left(1 + \frac{t}{\tau_c}\right)^{-2/7}, \tag{B2}$$

where τ_c is defined in equation (1) and T_0 is the temperature in the strand immediately following the nanoflare.

As conductive cooling proceeds, the temperature falls and the density rises, so that the instantaneous conductive cooling time gets longer and the radiative time becomes shorter. When the two cooling times are equal, there is a transition to radiative cooling that is described using the solution of Antiochos (1980),

$$T_e(t) = T_0\left[1 - \frac{3}{2}\left(\frac{1}{2} - \beta\right)\frac{t}{\tau_r}\right]^{1/(1/2-\beta)}, \tag{B3}$$

and the well-known result from the radiative-decay phase of flares that $T_e \propto N_e^2$ (see Cargill et al. 1995). Here β is the power of T_e in the radiative loss function of Figure 2, τ_r is defined in equation (1), and T_0 is now the temperature at the start of the radiative phase.

REFERENCES

Aletti, V., Velli, M., Bocchialini, K., Einaudi, G., Georgoulis, M., & Vial, J.-C. 2000, ApJ, 544, 550
Antiochos, S. K. 1980, ApJ, 241, 385
Antiochos, S. K., & Sturrock, P. A. 1978, ApJ, 220, 1137
Aschwanden, M. J., Nightingale, R. W., & Alexander, D. 2000, ApJ, 541, 1059
Aschwanden, M. J., & Parnell, C. E. 2002, ApJ, 572, 1048
Berghmans, D., Clette, F., & Moses, D. 1998, A&A, 336, 1039
Bradshaw, S. J., & Cargill, P. J. 2005, A&A, 437, 311
Buchlin, E., Aletti, V., Galtier, S., Velli, M., Einaudi, G., & Vial, J.-C. 2003, A&A, 406, 1061
Buchlin, E., Vial, J.-C., & Lemaire, P. 2006, A&A, 451, 1091
Cargill, P. J. 1994, ApJ, 422, 381
Cargill, P. J., & Klimchuk, J. A. 1997, ApJ, 478, 799
———. 2004, ApJ, 605, 911
Cargill, P. J., Mariska, J. T., & Antiochos, S. K. 1995, ApJ, 439, 1034
Crosby, N. B., Aschwanden, M. J., & Dennis, B. R. 1993, Sol. Phys., 143, 275
Delaboudiniere, J.-P., et al. 1995, Sol. Phys., 162, 291
Einaudi, G., & Velli, M. 1999, Phys. Plasmas, 6, 4146
Gudiksen, B. V., & Nordlund, Å. 2005, ApJ, 618, 1020
Hudson, H. S. 1991, Sol. Phys., 133, 357
Klimchuk, J. A. 2006, Sol. Phys., 234, 41
Lin, R. P., Schwartz, R. A., Kane, S. R., Pelling, R. M., & Hurley, K. C. 1984, ApJ, 283, 421
Lu, E. T., & Hamilton, R. J. 1991, ApJ, 380, L89
Mandrini, C. H., Démoulin, P., & Klimchuk, J. A. 2000, ApJ, 530, 999
Mazzotta, P., Mazzitelli, G., Colafrancesco, S., & Vittorio, N. 1998, A&AS, 133, 403
Mendoza-Briceño, C. A., Erdélyi, R., & Sigalotti, L. D. G. 2004, ApJ, 605, 493
Mendoza-Briceño, C. A., Sigalotti, L. D. G., & Erdélyi, R. 2005, ApJ, 624, 1080
Parker, E. N. 1988, ApJ, 330, 474
Parnell, C. E. 2004, in Proc. *SOHO* 15 Workshop: Coronal Heating (ESA SP-575; Noordwijk: ESA), 227
Parnell, C. E., & Jupp, P. E. 2000, ApJ, 529, 554
Patsourakos, S., & Klimchuk, J. A. 2006, ApJ, 647, 1452
Patsourakos, S., Klimchuk, J. A., & MacNeice, P. J. 2004, ApJ, 603, 322
Peres, G. 2000, Sol. Phys., 193, 33
Peter, H., Gudiksen, B. V., & Nordlund, Å. 2004, ApJ, 617, L85
Reale, F., Nigro, G., Malara, F., Peres, G., & Veltri, P. 2005, ApJ, 633, 489
Testa, P., Peres, G., & Reale, F. 2005, ApJ, 622, 695
Walsh, R. W., & Galtier, S. 2000, Sol. Phys., 197, 57
Wilhelm, K., et al. 1995, Sol. Phys., 162, 189
Winebarger, A. R., & Warren, H. P. 2004, ApJ, 610, L129
Young, P. R., Del Zanna, G., Landi, E., Dere, K. P., Mason, H. E., & Landini, M. 2003, ApJS, 144, 135